

A Fast Algorithm for Cosine Transform Based Tensor Singular Value Decomposition

Wen-Hao Xu^a, Xi-Le Zhao^{a,*}, Michael Ng^b

^a*School of Mathematical Sciences, University of Electronic Science and Technology of China, Chengdu, Sichuan, 611731, P. R. China*

^b*Department of Mathematics, Hong Kong Baptist University, Kowloon Tong, Hong Kong*

Abstract

Recently, there has been a lot of research into tensor singular value decomposition (t-SVD) by using discrete Fourier transform (DFT) matrix. The main aims of this paper are to propose and study tensor singular value decomposition based on the discrete cosine transform (DCT) matrix. The advantages of using DCT are that (i) the complex arithmetic is not involved in the cosine transform based tensor singular value decomposition, so the computational cost required can be saved; (ii) the intrinsic reflexive boundary condition along the tubes in the third dimension of tensors is employed, so its performance would be better than that by using the periodic boundary condition in DFT. We demonstrate that the tensor product between two tensors by using DCT can be equivalent to the multiplication between a block Toeplitz-plus-Hankel matrix and a block vector. Numerical examples of low-rank tensor completion are further given to illustrate that the efficiency by using DCT is two times faster than that by using DFT and also the errors of video and multispectral image completion by using DCT are smaller than those by using DFT.

Keywords: boundary condition, discrete cosine transform, discrete Fourier transform, tensor completion, tensor singular value decomposition.

1. Introduction

A tensor is a multi-dimensional array of numbers, which is a generalization of a matrix. Compared to a “flat” matrix, a tensor provides a richer and more natural representation for many data. In this paper, we focus on the third-order tensor which looks like a magic cube. This format of data is widely used in color image and gray-scale video inpainting [1–6], hyperspectral image (HSI) data recovery [7–10], personalized web search [11], high-order web link analysis [12], magnetic resonance imaging (MRI) data recovery [13], and seismic data reconstruction [14].

Like the matrix decomposition, the tensor decomposition is an important multilinear algebra tool. There are many different tensor decompositions. The CANDECOMP/PAAEAFAC (CP) decomposition [15] and the Tucker decomposition [16] are the two most well-known ones. The CP decomposition can be considered as the higher order generalization of the matrix singular value decomposition (SVD). It tries to decompose a tensor into a sum of rank-one tensors. Similar to the rank-one matrix, third-order rank-one tensors can be written as the outer product of 3 vectors. The CP-rank of a tensor is defined as the minimum number of rank-one tensors whose sum generates the

*Corresponding author

Email addresses: seanxwh@gmail.com (Wen-Hao Xu), xlzhao122003@163.com (Xi-Le Zhao), mng@math.hkbu.edu.hk (Michael Ng)

original tensor. This definition is an analog of the definition of matrix rank. The Tucker decomposition is the higher order generalization of the principal component analysis (PCA). It decomposes a tensor into a core tensor multiplied by a matrix along each mode. The Tucker rank based on Tucker decomposition is a vector whose i -th element is the mode- i unfolding matrix rank.

Recent years, Kilmer and Martin [17–19] proposed a third-order tensor decomposition called tensor singular value decomposition (t-SVD). This decomposition strategy is based on the definition of the tensor product (see Section 2). After performing one-dimensional discrete Fourier transformation (DFT) on the third dimension of the tensor, this tensor product makes tensor decomposition be an analog of matrix decomposition. This strategy avoids the loss of structure information in matricization of the tensor. But because of performing one-dimensional DFT on the third dimension, the obtained tensor is a complex tensor. These complex numbers lead to higher computational cost and are not required. Why don't we use another transformation instead of DFT to avoid its disadvantage? Discrete cosine transformation (DCT) [20] is the first alternative which expresses a finite sequence in terms of a sum of the cosine functions.

DCT only produces the real number for real input. This feature greatly reduces the data in the process of t-SVD, thus saving a lot of time. And there is another difference: DFT implies periodic boundary conditions (BC) when DCT implies reflexive BCs which yields a continuous extension at the boundaries [20]. If the signal satisfies reflexive BCs (real data often satisfies), the new t-SVD based on DCT can achieve better results than DFT. We give the theoretical derivation of using DCT for t-SVD and verify the superiority compared to DFT.

The rest of this paper is as follows. In Section 2, we introduce some related notations and the original t-SVD with DFT background. In Section 3, we propose the theoretical derivation of new t-SVD with DCT. Based on the new t-SVD, we introduce the new tensor nuclear norm in Section 4. We conduct extensive experiments to demonstrate the effectiveness of the proposed method in Section 5. In Section 6, we give some concluding remarks.

2. Notations and Preliminaries

In this section, we introduce the basic notations and give the definitions related to the t-SVD. We use non-bold lowercase letters for scalars, e.g., x , boldface lowercase letters for vectors, e.g., \mathbf{x} , boldface capital letters for matrices, e.g., \mathbf{X} , boldface Calligraphy letters for tensors, e.g., \mathcal{X} . \mathbb{R} and \mathbb{C} represent the field of real number and complex number, respectively. For a third-order tensor \mathcal{X} , we use the MATLAB notations $\mathcal{X}(i, :, :)$, $\mathcal{X}(:, j, :)$, and $\mathcal{X}(:, :, k)$ to denote the horizontal, lateral, and frontal slices, respectively, and $\mathcal{X}(:, j, k)$, $\mathcal{X}(i, :, k)$, and $\mathcal{X}(i, j, :)$ to denote the columns, rows, and tubes, respectively. For convenience, we use $\mathbf{X}^{(k)}$ for the k th **frontal slice** and $\mathbf{x}_{ij\cdot}$ for the (i, j) -th **tube** $\mathcal{X}(i, j, :)$. Both $\mathcal{X}(i, j, k)$ and x_{ijk} represent the (i, j, k) -th element. The Frobenius norm of \mathcal{X} is defined as $\|\mathcal{X}\|_F := (\sum_{i,j,k} |x_{ijk}|^2)^{\frac{1}{2}}$. It is easily to see that $\|\mathcal{X}\|_F^2 = \sum_{n=1}^k \|\mathbf{X}^{(n)}\|_F^2$.

Next, we introduce some definitions that are closely related to t-SVD. We use $\tilde{\mathcal{X}} \in \mathbb{C}^{m_1 \times m_2 \times m_3}$ to represent the discrete Fourier transform of $\mathcal{X} \in \mathbb{C}^{m_1 \times m_2 \times m_3}$ along each tube, i.e., $\tilde{\mathcal{X}} = \text{fft}(\mathcal{X}, [], 3)$. The block circulant matrix [18, 19] is defined as

$$\text{bcirc}(\mathcal{X}) := \begin{bmatrix} \mathbf{X}^{(1)} & \mathbf{X}^{(m_3)} & \dots & \mathbf{X}^{(2)} \\ \mathbf{X}^{(2)} & \mathbf{X}^{(1)} & \dots & \mathbf{X}^{(3)} \\ \vdots & \vdots & \ddots & \vdots \\ \mathbf{X}^{(m_3)} & \mathbf{X}^{(m_3-1)} & \dots & \mathbf{X}^{(1)} \end{bmatrix}. \quad (1)$$

The block diagonal matrix and the corresponding inverse operator [18, 19] are defined as

$$\text{bdiag}(\mathcal{X}) := \begin{bmatrix} \mathbf{X}^{(1)} & & & \\ & \mathbf{X}^{(2)} & & \\ & & \ddots & \\ & & & \mathbf{X}^{(m_3)} \end{bmatrix}, \quad (2)$$

$$\text{unbdiag}(\text{bdiag}(\mathcal{X})) = \mathcal{X}.$$

The unfold and fold operators in t-SVD [18, 19] are defined as

$$\text{unfold}(\mathcal{X}) := \begin{bmatrix} \mathbf{X}^{(1)} \\ \mathbf{X}^{(2)} \\ \vdots \\ \mathbf{X}^{(m_3)} \end{bmatrix}, \quad \text{fold}(\text{unfold}(\mathcal{X})) = \mathcal{X}. \quad (3)$$

It is a important point that block circulant matrix can be block diagonalized.

Theorem 1 ([17])

$$\text{bdiag}(\tilde{\mathcal{X}}) = (\mathbf{F}_{m_3} \otimes \mathbf{I}_{m_1}) \text{bcirc}(\mathcal{X}) (\mathbf{F}_{m_3}^H \otimes \mathbf{I}_{m_2}), \quad (4)$$

where \otimes denotes the Kronecker product, \mathbf{F}_{m_3} is an $m_3 \times m_3$ DFT matrix and \mathbf{I}_m is an $m \times m$ identity matrix.

Definition 1 (t-product [19]) Given $\mathcal{X} \in \mathbb{C}^{m_1 \times m_2 \times m_3}$ and $\mathcal{Y} \in \mathbb{C}^{m_2 \times m_4 \times m_3}$, the t-product $\mathcal{X} * \mathcal{Y}$ is a third-order tensor of size $m_1 \times m_4 \times m_3$

$$\mathcal{Z} = \mathcal{X} * \mathcal{Y} := \text{fold}(\text{bcirc}(\mathcal{X}) \text{unfold}(\mathcal{Y})). \quad (5)$$

This definition is the core of t-SVD. It is like a one-dimensional convolution of two vectors under reflexive BCs, but the elements of vectors are the frontal slices of tensors. With Theorem 1, equation (5) can be rewritten as

$$\begin{aligned} \tilde{\mathcal{Z}} &= \text{fold}(\text{bdiag}(\tilde{\mathcal{X}})((\mathbf{F}_{m_3} \otimes \mathbf{I}_{m_2}) \text{unfold}(\mathcal{Y}))) \\ &= \text{fold}(\text{bdiag}(\tilde{\mathcal{X}}) \text{unfold}(\tilde{\mathcal{Y}})) \\ &= \text{unbdiag}(\text{bdiag}(\tilde{\mathcal{X}}) \text{bdiag}(\tilde{\mathcal{Y}})). \end{aligned} \quad (6)$$

Equation (6) means that the t-product in the spatial domain corresponds to the matrix multiplication of the frontal slices in the Fourier domain, which greatly simplifies the process of the algorithm.

Definition 2 (identity tensor [19]) The identity tensor $\mathcal{I} \in \mathbb{C}^{m_1 \times m_1 \times m_3}$ is a tensor whose first frontal slice is the identity matrix of size $m_1 \times m_1$, and whose other frontal slices are all zeros.

Definition 3 (orthogonal tensor [19]) A tensor $\mathcal{Q} \in \mathbb{C}^{m_1 \times m_1 \times m_3}$ is orthogonal if it satisfies $\mathcal{Q} * \mathcal{Q}^H = \mathcal{Q}^H * \mathcal{Q} = \mathcal{I}$, where \mathcal{Q}^H is the tensor conjugate transpose of \mathcal{Q} , which is obtained by conjugate transposing each frontal slice of \mathcal{Q} .

Definition 4 (f-diagonal tensor [19]) A tensor is called f-diagonal if each of its frontal slices is a diagonal matrix.

Theorem 2 (t-SVD [17, 19]) Given a tensor $\mathcal{X} \in \mathbb{C}^{m_1 \times m_2 \times m_3}$, the t-SVD of \mathcal{X} is given by

$$\mathcal{X} = \mathcal{U} * \mathcal{S} * \mathcal{V}^H, \quad (7)$$

where $\mathcal{U} \in \mathbb{C}^{m_1 \times m_1 \times m_3}$, $\mathcal{V} \in \mathbb{C}^{m_2 \times m_2 \times m_3}$ are orthogonal tensors, and $\mathcal{S} \in \mathbb{C}^{m_1 \times m_2 \times m_3}$ is a f-diagonal tensor.

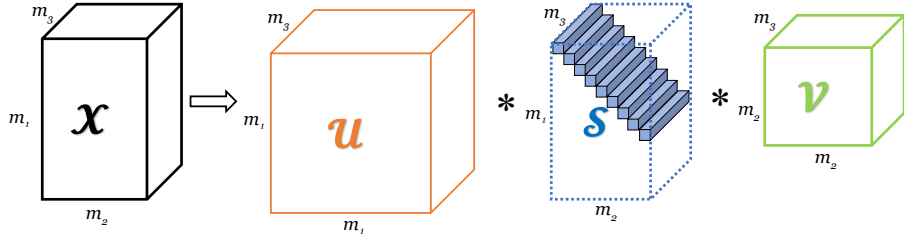


Figure 1: the t-SVD of an $m_1 \times m_2 \times m_3$ tensor.

Definition 5 (tensor multi-rank and tubal rank [21]) *Given $\mathcal{X} \in \mathbb{C}^{m_1 \times m_2 \times m_3}$, its multi-rank is a vector $\mathbf{r} \in \mathbb{R}^{m_3}$ whose i -th element is the rank of the i -th frontal slice of $\tilde{\mathcal{X}}$, i.e., $\mathbf{r}_i = \text{rank}(\tilde{\mathcal{X}}^{(i)})$. Its tubal rank is defined as the number of nonzero singular tubes, where the singular tubes of \mathcal{X} are the nonzero tubes of \mathcal{S} .*

The tensor tubal rank is actually the largest element of multi-rank.

Definition 6 (tensor nuclear norm [22, 23]) *Given $\mathcal{X} \in \mathbb{C}^{m_1 \times m_2 \times m_3}$, based on the tensor multi-rank, the tensor nuclear norm (TNN) of \mathcal{X} is defined as*

$$\|\mathcal{X}\|_* := \frac{1}{m_3} \sum_{k=1}^{m_3} \left\| \tilde{\mathbf{X}}^{(k)} \right\|_* . \quad (8)$$

In order to avoid confusion with the new definition of TNN we proposed later, we call this definition TNN-F in this paper.

The computation of t-SVD on an $m_1 \times m_2 \times m_3$ tensor needs two steps. Firstly, the first step is to perform DFT by fast Fourier transformation (FFT) along each tube. The time complexity of the first step is $O(m_1 m_2 m_3 \log(m_3))$. After DFT, the obtained tensor is a complex tensor which can be divided into a real number tensor and an imaginary number tensor. The computation of SVD along each frontal slice on the obtained tensor is actually equivalent to performing on the real number tensor and the imaginary number tensor respectively. The time complexity of the second step is $O(2m_3 \min(m_1 m_2^2, m_2 m_1^2))$, which is about the computational cost of the first step.

3. Cosine Transform Based Tensor Singular Value Decomposition

We discuss the DCT-based t-SVD and the resulting structure in this section. Since the corresponding block circulant matrices can be diagonalized by DFT, the DFT based t-SVD can be efficiently implemented via fast Fourier transform (fft). We will show the corresponding structure of DCT-based t-SVD can be diagonalized by DCT.

We define the shift of tensor \mathcal{A} = fold $\begin{bmatrix} \mathbf{A}^{(1)} \\ \mathbf{A}^{(2)} \\ \vdots \\ \mathbf{A}^{(m_3)} \end{bmatrix}$ as $\sigma(\mathcal{A})$ = fold $\begin{bmatrix} \mathbf{A}^{(2)} \\ \mathbf{A}^{(3)} \\ \vdots \\ \mathbf{A}^{(m_3)} \\ \mathbf{O} \end{bmatrix}$. It is easy to prove

that any tensor \mathcal{X} can be uniquely divided into $\mathcal{A} + \sigma(\mathcal{A})$. We use $\tilde{\mathcal{X}} \in \mathbb{R}^{m_1 \times m_2 \times m_3}$ to represent the DCT along each tube of \mathcal{X} , i.e., $\tilde{\mathcal{X}} = \text{dct}(\mathcal{X}, [], 3) = \text{dct}(\mathcal{A} + \sigma(\mathcal{A}), [], 3)$. We define the block

Toeplitz matrix of \mathcal{A} as

$$\text{bt}(\mathcal{A}) := \begin{bmatrix} \mathbf{A}^{(1)} & \mathbf{A}^{(2)} & \dots & \mathbf{A}^{(m_3-1)} & \mathbf{A}^{(m_3)} \\ \mathbf{A}^{(2)} & \mathbf{A}^{(1)} & \dots & \mathbf{A}^{(m_3-2)} & \mathbf{A}^{(m_3-1)} \\ \vdots & \vdots & \ddots & \vdots & \vdots \\ \mathbf{A}^{(m_3-1)} & \mathbf{A}^{(m_3-2)} & \dots & \mathbf{A}^{(1)} & \mathbf{A}^{(2)} \\ \mathbf{A}^{(m_3)} & \mathbf{A}^{(m_3-1)} & \dots & \mathbf{A}^{(2)} & \mathbf{A}^{(1)} \end{bmatrix}. \quad (9)$$

The block Hankel matrix is defined as

$$\text{bh}(\mathcal{A}) := \begin{bmatrix} \mathbf{A}^{(2)} & \mathbf{A}^{(3)} & \dots & \mathbf{A}^{(m_3)} & \mathbf{O} \\ \mathbf{A}^{(3)} & \mathbf{A}^{(4)} & \dots & \mathbf{O} & \mathbf{A}^{(m_3)} \\ \vdots & \vdots & \ddots & \vdots & \vdots \\ \mathbf{A}^{(m_3)} & \mathbf{O} & \dots & \mathbf{A}^{(4)} & \mathbf{A}^{(3)} \\ \mathbf{O} & \mathbf{A}^{(m_3)} & \dots & \mathbf{A}^{(3)} & \mathbf{A}^{(2)} \end{bmatrix}. \quad (10)$$

The block Toeplitz-plus-Hankel matrix of \mathcal{A} is defined as

$$\text{btp}(\mathcal{A}) := \text{bt}(\mathcal{A}) + \text{bh}(\mathcal{A}). \quad (11)$$

The block Toeplitz-plus-Hankel matrix can be diagonalized. The following theorem can be similarly established as [20].

Theorem 3

$$\text{bdiag}(\bar{\mathcal{X}}) = (\mathbf{C}_{m_3} \otimes \mathbf{I}_{m_1}) \text{btp}(\mathcal{A}) (\mathbf{C}_{m_3}^T \otimes \mathbf{I}_{m_2}), \quad (12)$$

where \otimes denotes the Kronecker product, \mathbf{C}_{m_3} is an $m_3 \times m_3$ DCT matrix.

The proof of Theorem 3 can be obtained by using the similar argument in [20]. We briefly illustrate this theorem with an example.

Example 1 Let the frontal slice of $\mathcal{X} \in \mathbb{R}^{2 \times 2 \times 2}$ be

$$\mathbf{X}^{(1)} = \begin{bmatrix} 1 & 2 \\ 3 & 4 \end{bmatrix}, \quad \mathbf{X}^{(2)} = \begin{bmatrix} 5 & 6 \\ 7 & 8 \end{bmatrix}.$$

So the component \mathcal{A} is

$$\mathbf{A}^{(1)} = \mathbf{X}^{(1)} - \mathbf{X}^{(2)} = \begin{bmatrix} -4 & -4 \\ -4 & -4 \end{bmatrix}, \quad \mathbf{A}^{(2)} = \mathbf{X}^{(2)} = \begin{bmatrix} 5 & 6 \\ 7 & 8 \end{bmatrix}.$$

The block Toeplitz matrix is

$$\text{bt}(\mathcal{A}) = \begin{bmatrix} \mathbf{A}^{(1)} & \mathbf{A}^{(2)} \\ \mathbf{A}^{(2)} & \mathbf{A}^{(1)} \end{bmatrix} = \begin{bmatrix} -4 & -4 & 5 & 6 \\ -3 & -4 & 7 & 8 \\ 5 & 6 & -4 & -4 \\ 7 & 8 & -4 & -4 \end{bmatrix},$$

and the block Hankel matrix is

$$\text{bh}(\mathcal{A}) = \begin{bmatrix} \mathbf{A}^{(2)} & 0 \\ 0 & \mathbf{A}^{(2)} \end{bmatrix} = \begin{bmatrix} 5 & 6 & 0 & 0 \\ 7 & 8 & 0 & 0 \\ 0 & 0 & 5 & 6 \\ 0 & 0 & 7 & 8 \end{bmatrix}.$$

Then the block Toeplitz-plus-Hankel matrix is

$$btph(\mathcal{A}) = bt(\mathcal{A}) + bh(\mathcal{A}) = \begin{bmatrix} 1 & 2 & 5 & 6 \\ 3 & 4 & 7 & 8 \\ 5 & 6 & 1 & 2 \\ 7 & 8 & 3 & 4 \end{bmatrix}.$$

By using stride permutations, we get

$$\mathbf{P}btph(\mathcal{A})\mathbf{P} = \begin{bmatrix} 1 & 5 & 2 & 6 \\ 5 & 1 & 6 & 2 \\ 3 & 7 & 4 & 8 \\ 7 & 3 & 8 & 4 \end{bmatrix} = \begin{bmatrix} \mathbf{A} & \mathbf{B} \\ \mathbf{C} & \mathbf{D} \end{bmatrix},$$

where $\mathbf{P} = \begin{bmatrix} 1 & 0 & 0 & 0 \\ 0 & 0 & 1 & 0 \\ 0 & 1 & 0 & 0 \\ 0 & 0 & 0 & 1 \end{bmatrix}$ and \mathbf{A} , \mathbf{B} , \mathbf{C} , and \mathbf{D} are Toeplitz-plus-Hankel matrices. So we have

$$(\mathbf{C}_2 \otimes \mathbf{I}_2)btph(\mathcal{A})(\mathbf{C}_2^T \otimes \mathbf{I}_2) = (\mathbf{C}_2 \otimes \mathbf{I}_2)\mathbf{P}\mathbf{P}btph(\mathcal{A})\mathbf{P}\mathbf{P}(\mathbf{C}_2^T \otimes \mathbf{I}_2),$$

where \mathbf{C}_2 is a 2×2 DCT matrix. In this equation, it is easy to see that

$$\mathbf{P}(\mathbf{C}_2 \otimes \mathbf{I}_2)\mathbf{P} = \begin{bmatrix} \mathbf{C}_2 & 0 \\ 0 & \mathbf{C}_2 \end{bmatrix}.$$

Similarly,

$$\mathbf{P}(\mathbf{C}_2^T \otimes \mathbf{I}_2)\mathbf{P} = \begin{bmatrix} \mathbf{C}_2^T & 0 \\ 0 & \mathbf{C}_2^T \end{bmatrix}.$$

Hence, we have

$$\begin{aligned} (\mathbf{C}_2 \otimes \mathbf{I}_2)btph(\mathcal{A})(\mathbf{C}_2^T \otimes \mathbf{I}_2) &= \mathbf{P} \begin{bmatrix} \mathbf{C}_2 & 0 \\ 0 & \mathbf{C}_2 \end{bmatrix} \begin{bmatrix} \mathbf{A} & \mathbf{B} \\ \mathbf{C} & \mathbf{D} \end{bmatrix} \begin{bmatrix} \mathbf{C}_2^T & 0 \\ 0 & \mathbf{C}_2^T \end{bmatrix} \mathbf{P} \\ &= \mathbf{P} \begin{bmatrix} \mathbf{C}_2 \mathbf{A} \mathbf{C}_2^T & \mathbf{C}_2 \mathbf{B} \mathbf{C}_2^T \\ \mathbf{C}_2 \mathbf{C} \mathbf{C}_2^T & \mathbf{C}_2 \mathbf{D} \mathbf{C}_2^T \end{bmatrix} \mathbf{P} \\ &= \begin{bmatrix} 6 & 8 & 0 & 0 \\ 10 & 12 & 0 & 0 \\ 0 & 0 & -4 & -4 \\ 0 & 0 & -4 & -4 \end{bmatrix}. \end{aligned}$$

Now, it is easy to verify

$$\begin{aligned} bdiag(\bar{\mathcal{X}}) &= bdiag(dct(\mathcal{A} + \sigma(\mathcal{A}), [], 3)) \\ &= (\mathbf{C}_2 \otimes \mathbf{I}_2)btph(\mathcal{A})(\mathbf{C}_2^T \otimes \mathbf{I}_2). \end{aligned}$$

Definition 7 (DCT-based t-product) Given $\mathcal{X} \in \mathbb{C}^{m_1 \times m_2 \times m_3}$ and $\mathcal{Y} \in \mathbb{C}^{m_2 \times m_4 \times m_3}$, the t-product $\mathcal{X} * \mathcal{Y}$ is a third-order tensor of size $m_1 \times m_4 \times m_3$

$$\mathcal{Z} = \mathcal{X} * \mathcal{Y} := \text{fold}(btph(\mathcal{A})\text{unfold}(\mathcal{Y})), \quad (13)$$

where $\mathcal{X} = \mathcal{A} + \sigma(\mathcal{A})$.

Equation (13) can be rewritten as

$$\begin{aligned} \bar{\mathcal{Z}} &= \text{fold}(\text{bdiag}(\bar{\mathcal{X}})((\mathbf{C}_{m_3} \otimes \mathbf{I}_{m_2})\text{unfold}(\mathcal{Y}))) \\ &= \text{fold}(\text{bdiag}(\bar{\mathcal{X}})\text{unfold}(\bar{\mathcal{Y}})). \end{aligned} \quad (14)$$

Based on this new t-product, the DCT-based t-SVD can be defined as follows:

Theorem 4 (DCT-based t-SVD) *Given a tensor $\mathcal{X} \in \mathbb{R}^{m_1 \times m_2 \times m_3}$, the DCT-based t-SVD of \mathcal{X} is given by*

$$\mathcal{X} = \mathcal{U} * \mathcal{S} * \mathcal{V}^T, \quad (15)$$

where $\mathcal{U} \in \mathbb{R}^{m_1 \times m_1 \times m_3}, \mathcal{V} \in \mathbb{R}^{m_2 \times m_2 \times m_3}$ are orthogonal tensors, $\mathcal{S} \in \mathbb{R}^{m_1 \times m_2 \times m_3}$ is a f-diagonal tensor, and \mathcal{V}^T is the tensor transpose of \mathcal{V} , which is obtained by transposing each frontal slice of \mathcal{V} .

The proof of Theorem 4 can be obtained by using the similar argument in [19].

By exploiting the beautiful structure, the DCT-based t-SVD can be efficiently calculated by performing the matrix singular value decomposition for each frontal slice of the third-order tensor after DCT along each tube. For an $m_1 \times m_2 \times m_3$ tensor, the time complexity of performing DCT along each tube in the first step is $O(m_1 m_2 m_3 \log(m_3))$ for DCT-based t-SVD, which is the same as that DFT-based t-SVD. Since DCT only produces the real number, the time complexity of calculating SVDs is $O(m_3 \min(m_1 m_2^2, m_2 m_1^2))$ for DCT-based t-SVD, which is half that of DFT-based t-SVD.

Table 1: The time complexity of t-SVD and DCT-based t-SVD on an $m_1 \times m_2 \times m_3$ tensor.

tensor	$m_1 \times m_2 \times m_3$
DFT	$O(m_1 m_2 m_3 \log(m_3))$
SVD after DFT	$O(2m_3 \min(m_1 m_2^2, m_2 m_1^2))$
t-SVD	$O(m_1 m_2 m_3 \log(m_3)) + O(2m_3 \min(m_1 m_2^2, m_2 m_1^2))$
DCT	$O(m_1 m_2 m_3 \log(m_3))$
SVD after DCT	$O(m_3 \min(m_1 m_2^2, m_2 m_1^2))$
new t-SVD	$O(m_1 m_2 m_3 \log(m_3)) + O(m_3 \min(m_1 m_2^2, m_2 m_1^2))$

4. Low-rank Tensor Completion by TNN-C

Based on the DCT-based t-SVD, we propose the new definition of TNN called TNN-C in this section. Then, we establish the low-rank tensor completion model [6] based on TNN-C and develop the alternating direction method of multipliers (ADMM) to tackle the corresponding low-rank tensor completion model.

Definition 8 (TNN-C) *Given $\mathcal{X} \in \mathbb{R}^{m_1 \times m_2 \times m_3}$, TNN-C of \mathcal{X} is defined as*

$$\|\mathcal{X}\|_* = \frac{1}{m_3} \sum_{i=1}^{m_3} \left\| \bar{\mathbf{X}}^{(i)} \right\|_*. \quad (16)$$

It is easy to see that TNN-C of \mathcal{X} is the sum of singular values of all frontal slices of $\bar{\mathcal{X}}$. Meanwhile, the i -th element of multi-rank is the rank of the i -th frontal slice of $\bar{\mathcal{X}}$. Thus, TNN-C is a convex surrogate of the l_1 norm of a third-order tensor's multi-rank.

The low-rank tensor completion model is defined as

$$\min_{\mathcal{X}} \|\mathcal{X}\|_*, \quad s.t. \quad \mathcal{X}_{\Omega} = \mathcal{B}_{\Omega}. \quad (17)$$

Letting

$$l_{\mathbb{S}}(\mathcal{X}) = \begin{cases} 0, & \text{if } \mathcal{X} \in \mathbb{S}, \\ \infty, & \text{otherwise,} \end{cases}$$

where $\mathbb{S} := \{\mathcal{X} \in \mathbb{R}^{m_1 \times m_2 \times m_3}, \mathcal{X}_{\Omega} = \mathcal{B}_{\Omega}\}$, (17) can be rewritten as the following unconstrained problem:

$$\min_{\mathcal{X}} \|\mathcal{X}\|_* + l_{\mathbb{S}}(\mathcal{X}). \quad (18)$$

By introducing an auxiliary variable $\mathcal{Y} = \mathcal{X}$, the augmented Lagrangian function of (18) is

$$\begin{aligned} L(\mathcal{X}, \mathcal{Y}, \mathcal{M}) &:= \|\mathcal{Y}\|_* + l_{\mathbb{S}}(\mathcal{X}) + \langle \mathcal{Y} - \mathcal{X}, \mathcal{M} \rangle + \frac{\beta}{2} \|\mathcal{Y} - \mathcal{X}\|_F^2 \\ &= \|\mathcal{Y}\|_* + l_{\mathbb{S}}(\mathcal{X}) + \frac{\beta}{2} \left\| \mathcal{Y} - \mathcal{X} + \frac{1}{\beta} \mathcal{M} \right\|_F^2 - \frac{1}{2\beta} \langle \mathcal{M}, \mathcal{M} \rangle, \end{aligned} \quad (19)$$

where $\mathcal{M} \in \mathbb{R}^{m_1 \times m_2 \times m_3}$ is the Lagrangian multiplier, and β is the balance parameter. According to the framework of ADMM [24–26], \mathcal{X} , \mathcal{Y} , and \mathcal{M} are iteratively updated as

$$\begin{cases} \text{Step 1: } \mathcal{Y}^{l+1} \in \arg \min_{\mathcal{Y}} L(\mathcal{X}^l, \mathcal{Y}, \mathcal{M}^l), \\ \text{Step 2: } \mathcal{X}^{l+1} \in \arg \min_{\mathcal{X}} L(\mathcal{X}, \mathcal{Y}^{l+1}, \mathcal{M}^l), \\ \text{Step 3: } \mathcal{M}^{l+1} = \mathcal{M}^l + \beta(\mathcal{Y}^{l+1} - \mathcal{X}^{l+1}). \end{cases} \quad (20)$$

Now, we give the details for solving each subproblem.

In **Step 1**, the \mathcal{Y} -subproblem is:

$$\arg \min_{\mathcal{Y}} \|\mathcal{Y}\|_* + \frac{\beta}{2} \left\| \mathcal{Y} - \mathcal{X}^l + \frac{1}{\beta} \mathcal{M}^l \right\|_F^2, \quad (21)$$

which can be solved by the following theorem [22, 23].

Theorem 5 *Given $\mathcal{Z} \in \mathbb{C}^{m_1 \times m_2 \times m_3}$, a minimizer to*

$$\min_{\mathcal{Y}} \|\mathcal{Y}\|_* + \frac{\beta}{2} \|\mathcal{Y} - \mathcal{Z}\|_F^2 \quad (22)$$

is given by the tensor singular value thresholding

$$\mathcal{Y} = \mathcal{U} * \mathcal{D}_{\frac{1}{\beta}} * \mathcal{V}^T, \quad (23)$$

*where $\mathcal{Z} = \mathcal{U} * \mathcal{S} * \mathcal{V}^T$ and $\mathcal{D}_{\frac{1}{\beta}}$ is an $\mathbb{R}^{m_1 \times m_2 \times m_3}$ f-diagonal tensor whose each frontal slice in the discrete cosine domain is $\bar{\mathcal{D}}_{\frac{1}{\beta}}(i, i, j) = (\bar{\mathcal{S}}(i, i, j) - \frac{1}{\beta})_+$.*

In **Step 2**, we solve the following problem:

$$\arg \min_{\mathcal{X}} l_{\mathbb{S}}(\mathcal{X}) + \frac{\beta}{2} \left\| \mathcal{Y}^{l+1} - \mathcal{X} + \frac{1}{\beta} \mathcal{M}^l \right\|_F^2, \quad (24)$$

which has a closed-form solution

$$\mathcal{X}^{l+1} = (\mathcal{Y}^{l+1} + \frac{1}{\beta} \mathcal{M}^l)_{\Omega^C} + \mathcal{B}, \quad (25)$$

where Ω^C is the complementary set of the index set Ω .

We summarize the proposed ADMM procedure in Algorithm 1. Every step of ADMM has an explicit solution. Thus, the proposed method is efficiently implementable. The convergence of the ADMM method of convex functions of separable variables with linear constraints is guaranteed [27, 28].

Algorithm 1 ADMM for solving the proposed model (17).

Input: Observed data \mathcal{B} , index set Ω , parameters β .
Initialize: $\mathcal{X} = \mathcal{B}$, $\mathcal{Y} = \mathbf{0}$, $\mathcal{M} = \mathbf{0}$, $\text{tol} = 10^{-5}$, and $L = 500$.

- 1: **while** $l < L$ and $\|\mathcal{X}^{l+1} - \mathcal{X}^l\|_F / \|\mathcal{X}^l\|_F > \text{tol}$ **do**
- 2: $\mathcal{Z} = \mathcal{X}^l - \frac{1}{\beta} \mathcal{M}^l$;
- 3: $\bar{\mathcal{Z}} = \text{dct}(\mathcal{Z}, [], 3)$;
- 4: **for** $k = 1$ to m_3 **do**
- 5: $[\bar{\mathbf{U}}^{(k)}, \bar{\mathbf{S}}^{(k)}, \bar{\mathbf{V}}^{(k)}] = \text{SVD}(\bar{\mathbf{Z}}^{(k)})$;
- 6: $\bar{\mathbf{D}}^{(k)} = (\bar{\mathbf{S}}^{(k)} - 1/\beta)_+$;
- 7: $\bar{\mathbf{Z}}^{(k),l+1} = \mathbf{U}^{(k)} \bar{\mathbf{D}}^{(k)} \mathbf{V}^{(k)H}$;
- 8: **end for**
- 9: $\mathcal{Y}^{l+1} = \text{idct}(\bar{\mathcal{Z}}^{l+1}, [], 3)$;
- 10: $\mathcal{X}^{l+1} = (\mathcal{Y}^{l+1} + \frac{1}{\beta} \mathcal{M}^l)_{\Omega^c} + \mathcal{B}$;
- 11: $\mathcal{M}^{l+1} = \mathcal{M}^l + \beta(\mathcal{Y}^{l+1} - \mathcal{X}^{l+1})$.
- 12: **end while**

Output: The recovered tensor \mathcal{X} .

5. Numerical Examples

In this section, all experiments are implemented on Windows 10 and Matlab (R2017a) with an Intel(R) Core(TM) i7-7700k CPU at 4.20 GHz and 16 GB RAM.

5.1. The Computational Time

Saving time is the most important advantage of DCT-based t-SVD. We illustrate this advantage of the new t-SVD by operating on random tensors. We set 4 groups of random tensors of different size and performed 1000 runs to get the average time required. Tab. 2 shows that average time cost of performing t-SVD and DCT-based t-SVD, and confirms our point that DCT-based t-SVD only needs half the time of t-SVD.

Table 2: The time cost of t-SVD and DCT-based t-SVD on the random tensors of different size.

size	100*100*100	100*100*400	200*200*100	400*400*100
FFT	0.0041	0.0175	0.0176	0.0653
SVD after FFT	0.0818	0.3250	0.3641	1.9015
original t-SVD	0.0859	0.3425	0.3817	1.9668
DCT	0.0042	0.0150	0.0162	0.0601
SVD after DCT	0.0439	0.1649	0.1978	0.8922
new t-SVD	0.0481	0.1799	0.2140	0.9523

5.2. Real Data

We conduct the video and multispectral image (MSI) completion experiments and compare TNN-C with the TNN-F [22]. In our experiments, the quality of the recovered image is measured by the average of highest peak signal-to-noise ratio (PSNR) and structural similarity index (SSIM) of all bands. PSNR of a band is defined as follows:

$$\text{PSNR} = 10 \log_{10} \frac{m_1 m_2 \mathbf{X}_{\max}^2}{\|\hat{\mathbf{X}} - \mathbf{X}\|_F^2},$$

where \mathbf{X} is the masked matrix, $\hat{\mathbf{X}}$ is the recovered matrix, and \mathbf{X}_{\max} is the maximum pixel value of the original matrix \mathbf{X} . SSIM can measure the similarity between the recovered image and the

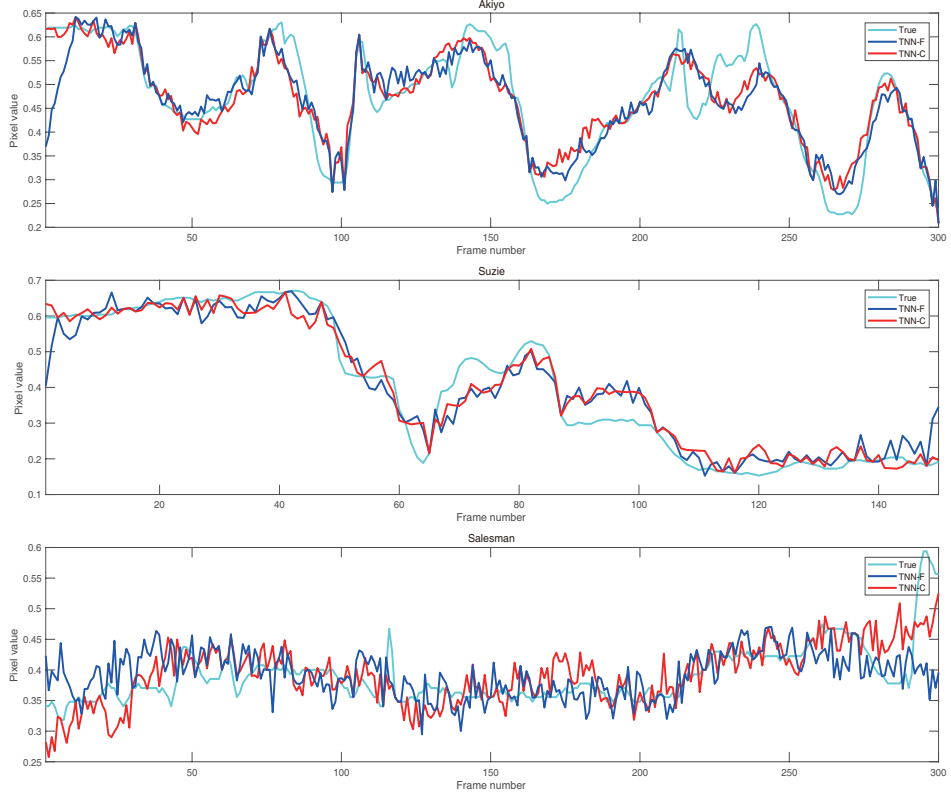


Figure 2: The pixel value of a selected tube of videos *Akiyo*, *Suzie*, and *Salesman*.

masked image. This indicator can reflect the similarities in brightness, contrast, and structure of two images and is defined as

$$\text{SSIM} = \frac{(2\mu_{\mathbf{x}}\mu_{\hat{\mathbf{x}}} + c_1)(2\sigma_{\mathbf{x}\hat{\mathbf{x}}} + c_2)}{(\mu_{\mathbf{x}}^2 + \mu_{\hat{\mathbf{x}}}^2 + c_1)(\sigma_{\mathbf{x}}^2 + \sigma_{\hat{\mathbf{x}}}^2 + c_1)},$$

where $\mu_{\mathbf{x}}$ and $\mu_{\hat{\mathbf{x}}}$ represent the average values of the original matrix and the estimated matrix, respectively, $\sigma_{\mathbf{x}}$ and $\sigma_{\hat{\mathbf{x}}}$ represent the standard deviation of \mathbf{X} and $\hat{\mathbf{X}}$, respectively.

For all the following experiments, we set the maximum number of iterations to 500 and the tolerance to 1×10^{-8} . This algorithm only needs one parameter β , and we set it to 1×10^{-2} .

Video completion. We test 3 videos: *Akiyo*, *Suzie*, and *Salesman*. The size of *Akiyo* and *Salesman* is $144 \times 176 \times 300$. The size of *Suzie* is $144 \times 176 \times 150$. Tab.3 shows PSNR, SSIM, and time cost of TNN-F and TNN-C. TNN-C achieves better results and costs much less time than TNN-F in all experiments. Fig.2 shows one selected tube. We can observe that the tube of recovered video by TNN-C is more closely to the true tube than that by TNN-F, especially near the boundary. Fig.3 shows the PSNR values of each frame of recovered videos by TNN-F and TNN-C. We can observe that when the sampling rate (SR) is 0.1, the PSNR values of TNN-C are higher than those of TNN-F, especially for the first and last few frames. This observation is consistent with our interpretation of BCs. Fig.4 shows the results recovered by TNN-F and TNN-C with SR = 0.1. TNN-C is visually better than TNN-F.

MSI completion. For MSI data, we add spectral angle mapper (SAM) and erreur relative globale adimensionnelle de synthèse (ERGAS) which are common quality metrics for MSI data. SAM calculates the angle in spectral space between pixels and a set of reference tensor on spectral

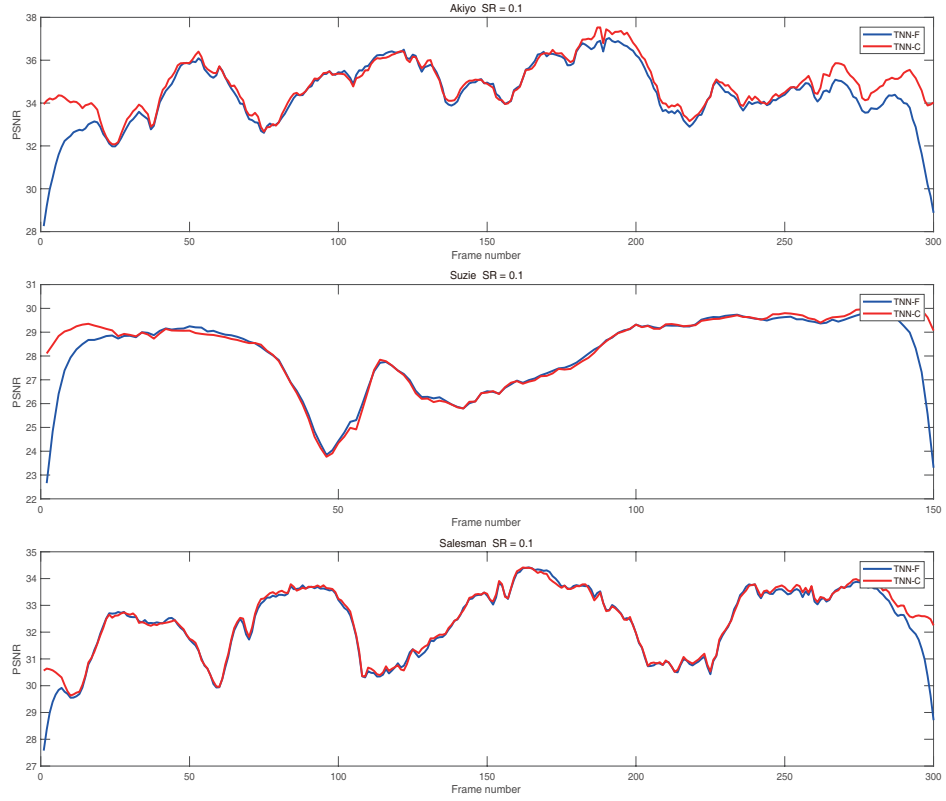


Figure 3: The PSNR values of each frame of the recovered videos *Akiyo*, *Suzie*, and *Salesman* obtained by TNN-F and TNN-C.

Table 3: PSNR, SSIM, and time of two methods in video completion. In brackets, they are the time required for transformation and time required for performing SVD. The best results are highlighted in bold.

video		<i>akiyo</i>		<i>suzie</i>		<i>salesman</i>	
SR	metric	TNN-F	TNN-C	TNN-F	TNN-C	TNN-F	TNN-C
0.05	PSNR	32.00	32.57	25.50	26.02	30.12	30.22
	SSIM	0.934	0.941	0.681	0.700	0.895	0.897
	time	156.2 (8.8+137.0)	91.9 (6.2+70.9)	69.6 (4.0+60.6)	40.1 (2.9+30.6)	148.5 (8.6+128.9)	85.6 (6.0+65.3)
0.1	PSNR	34.20	34.75	27.73	27.93	32.13	32.29
	SSIM	0.958	0.963	0.759	0.766	0.928	0.931
	time	141.8 (8.1+122.9)	86.3 (5.8+66.6)	64.5 (3.8+55.2)	39.3 (2.8+30.2)	139.5 (8.3+120.3)	84.9 (5.8+64.9)
0.2	PSNR	37.44	38.11	30.29	30.51	35.01	35.20
	SSIM	0.979	0.983	0.838	0.844	0.960	0.961
	time	145.2 (8.1+125.6)	79.8 (5.4+60.3)	62.5 (3.6+53.3)	37.2 (2.8+28.6)	135.1 (8.1+116.3)	81.3 (5.5+61.6)

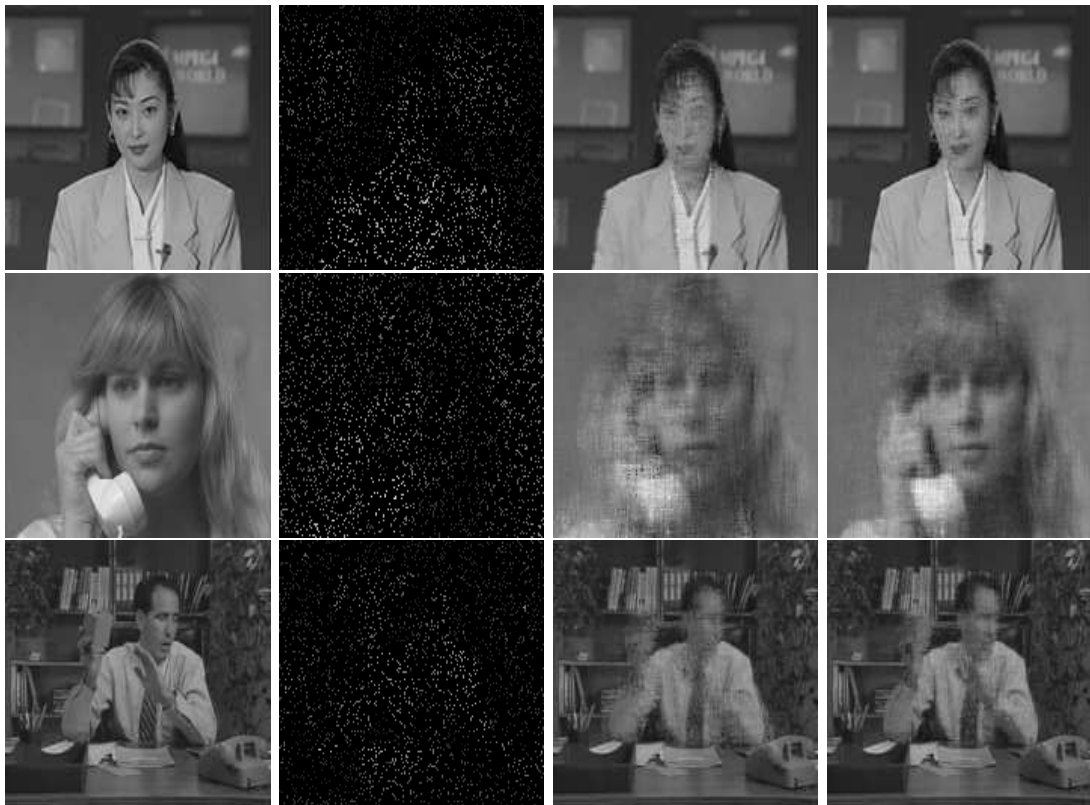


Figure 4: A frame of the recovered videos with $SR = 0.1$. From top to bottom: *Akiyo*, *Suzie*, and *Salesman*. From left to right: the original image, the masked image, the results by TNN-F, and TNN-C.

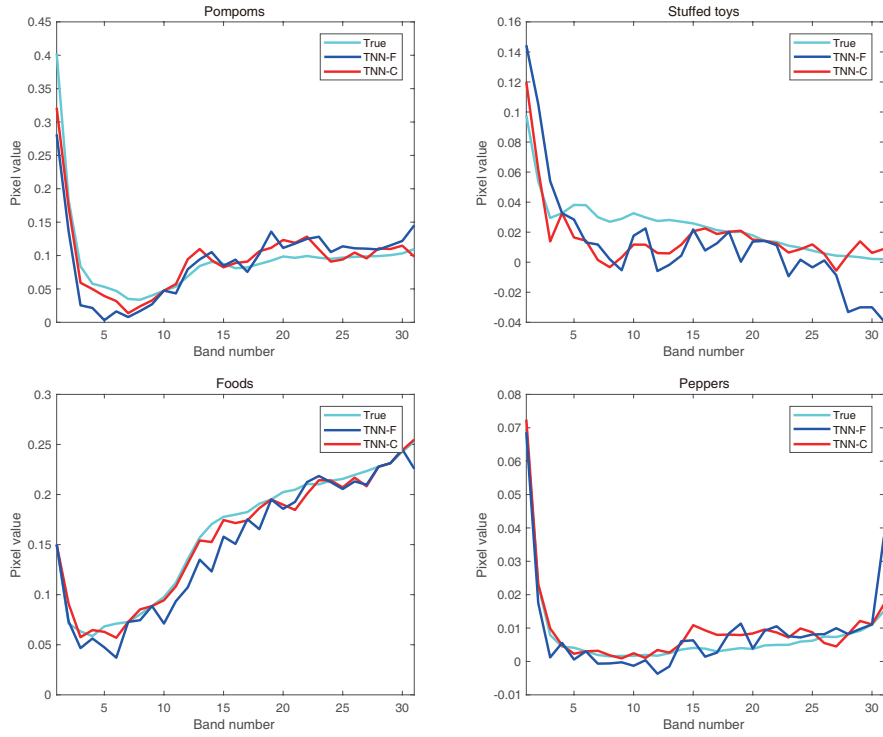


Figure 5: The pixel values of a random tube of MSI *Pompoms*, *Stuffed toys*, *Foods*, and *Peppers*.

similarity. ERGAS measures fidelity of the recovered tensor based on the weighted sum of mean squared error (MSE) of all bands. The lower the value of these two indicators, the better the results. The size of the MSI data from CAVE database is $512 \times 512 \times 31$ with the wavelengths in the range of $400 - 700$ nm at an interval of 10nm. We display one selected tube in Fig. 5. We can observe that the tube of recovered tensor by TNN-C is more closely to the true tube than that by TNN-F, especially near the boundary. Moreover, we plot the PSNR values of recovered tensor by TNN-C and TNN-F in Fig. 6. In general, we can observe that the PSNR values of TNN-C are higher than those of TNN-F, especially for the first and last few bands. Those observations verify TNN-C can produce more natural results as compared to TNN-F when more reasonable BCs is implied in TNN-C. In Fig. 7, we show the first band of testing data recovered by the two methods with SR = 0.1. Obviously, TNN-C achieves better visual results than TNN-F. Tabs. 4-5 give the more detailed data of other testing images. We can see that TNN-C not only has a better performance in PSNR, SSIM, SAM, and ERGAS, but also significantly reduces the time cost compared to TNN-F.

Parameter analysis. We analyze the robustness of TNN-C for different parameters using MSI data *Stuffed toys* with $SR = 0.1$. TNN-C only requires one parameter β . As shown in Fig. (8), different β lead to nearly the same PSNR value, but it affects the convergence speed. After testing, we choose $\beta = 1 \times 10^{-2}$ for all experiments.

6. Concluding Remarks

We have introduced the DCT as an alternative of DFT into the framework of t-SVD. Based on the resulting t-SVD, the DCT based tensor nuclear norm (TNN-C) is suggested for low-rank tensor completion problem. We have developed an efficient alternating direction method of multipliers

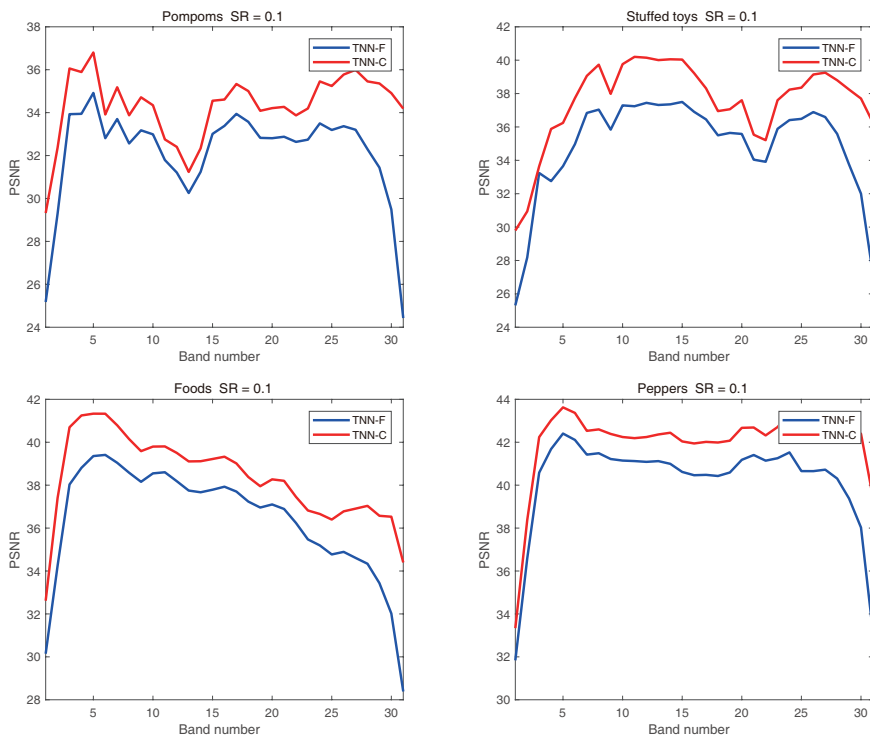


Figure 6: The PSNR values of each band of the recovered MSIs *Pompoms*, *Stuffed toys*, *Foods*, and *Peppers* obtained by TNN-F and TNN-C.

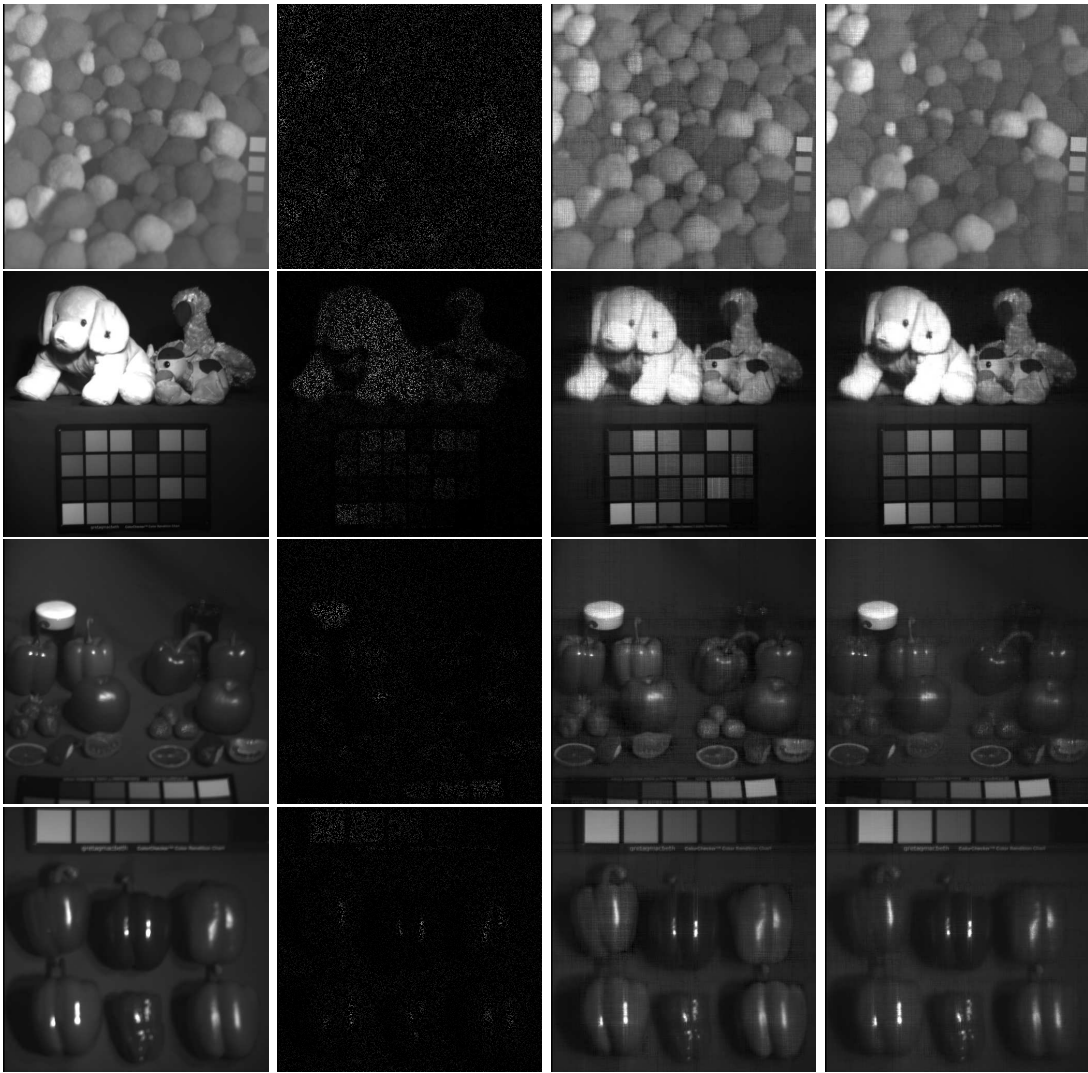


Figure 7: The first band of recovered MSI images with SR = 0.1. From top to bottom: *Pompoms*, *Stuffed toys*, *Foods*, and *Peppers*. From left to right: the original image, the masked image, the results by TNN-F, and TNN-C.

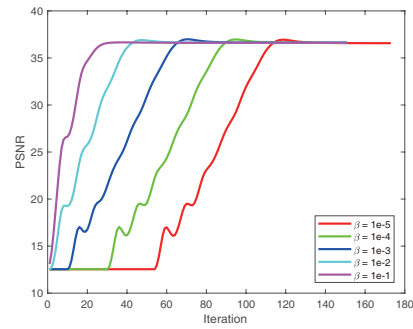


Figure 8: The PSNR values with respect to the iteration for different values of parameter β .

Table 4: PSNR, SSIM, SAM, ERGAS, and time of two methods in MSI completion. In brackets, they are time required for transformation and time required for performing SVD. The best results are highlighted in bold.

MSI		<i>Pompoms</i>		<i>Stuffed toys</i>	
SR	metric	TNN-F	TNN-C	TNN-F	TNN-C
0.05	PSNR	26.56	29.00	28.44	31.84
	SSIM	0.818	0.876	0.892	0.941
	SAM	0.22	0.16	0.30	0.22
	ERGAS	10.28	8.00	9.80	6.74
	time	309.4	161.0	320.6	183.4
		(11.0+285.7)	(8.9+135.3)	(11.4+296.0)	(10.3+153.4)
0.1	PSNR	31.26	33.98	33.37	36.63
	SSIM	0.922	0.952	0.955	0.978
	SAM	0.13	0.09	0.19	0.14
	ERGAS	5.96	4.52	5.53	3.84
	time	271.7	171.1	320.2	164.5
		(9.6+251.5)	(9.6+143.9)	(11.2+295.8)	(9.2+138.1)
0.2	PSNR	37.13	39.55	39.14	41.94
	SSIM	0.976	0.986	0.986	0.994
	SAM	0.07	0.05	0.11	0.09
	ERGAS	3.04	2.39	2.82	2.06
	time	308.1	184.0	278.9	165.8
		(10.9+284.4)	(10.2+154.2)	(10.2+256.4)	(9.2+138.7)

Table 5: PSNR, SSIM, SAM, ERGAS, and time of two methods in MSI completion. In brackets, they are time required for transformation and time required for performing SVD. The best results are highlighted in bold.

MSI		<i>Foods</i>		<i>Peppers</i>	
SR	metric	TNN-F	TNN-C	TNN-F	TNN-C
0.05	PSNR	31.48	33.33	34.89	36.87
	SSIM	0.904	0.932	0.946	0.965
	SAM	0.27	0.21	0.21	0.15
	ERGAS	9.52	8.01	6.31	5.21
	time	281.0	164.8	284.9	155.0
		(10.3+258.7)	(9.2+137.9)	(10.4+255.2)	(8.8+128.7)
0.1	PSNR	35.31	37.73	39.25	41.27
	SSIM	0.957	0.974	0.980	0.989
	SAM	0.18	0.13	0.13	0.09
	ERGAS	6.14	4.91	3.86	3.18
	time	291.4	167.7	278.3	146.8
		(10.7+267.9)	(9.4+140.2)	(10.0+256.6)	(8.6+124.9)
0.2	PSNR	43.13	40.30	44.30	46.22
	SSIM	0.993	0.986	0.995	0.997
	SAM	0.11	0.08	0.07	0.05
	ERGAS	3.49	2.68	2.19	1.82
	time	289.7	164.0	286.2	153.6
		(10.6+266.7)	(9.3+137.4)	(10.4+264.2)	(9.0+138.5)

(ADMM) to tackle the corresponding model. Numerical experiments are reported to demonstrate the superiority of the DCT-based t-SVD. In the future research work, other transforms based tensor singular value decomposition can be considered and studied. We expect other transforms based tensor singular value decomposition can deal with data tensors from specific applications.

Acknowledgment

The research is supported by NSFC (61772003) and the Fundamental Research Funds for the Central Universities (ZYGX2016J132), the HKRGC GRF 1202715, 12306616, 12200317 and HKBU RC-ICRS/16-17/03.

References

References

- [1] M. Bertalmio, G. Sapiro, V. Caselles, C. Ballester, Image inpainting, *Proceedings of International Conference on Computer Graphics and Interactive Techniques* (2000) 417–424 (2000).
- [2] N. Komodakis, Image completion using global optimization, *Proceedings of Computer Vision and Pattern Recognition* (2006) 442–452 (2006).
- [3] J. Liu, P. Musialski, P. Wonka, J.-P. Ye, Tensor completion for estimating missing values in visual data, *IEEE Transactions on Pattern Analysis and Machine Intelligence* 35 (1) (2013) 208–220 (2013).
- [4] T. Korah, C. Rasmussen, Spatiotemporal inpainting for recovering texture maps of occluded building facades, *IEEE Transactions on Image Processing* 16 (9) (2007) 2262–2271 (2007).
- [5] S. H. Chan, R. Khoshabeh, K. B. Gibson, P. E. Gill, T. Q. Nguyen, An augmented lagrangian method for total variation video restoration, *IEEE Transactions on Image Processing* 20 (11) (2011) 3097–3111 (2011).
- [6] T.-X. Jiang, T.-Z. Huang, X.-L. Zhao, L.-J. Deng, Y. Wang, A novel tensor-based video rain streaks removal approach via utilizing discriminatively intrinsic priors, *Proceedings of Computer Vision and Pattern Recognition* (2017) 2818–2827 (07 2017).
- [7] F. Li, M. K. Ng, R. J. Plemmons, Coupled segmentation and denoising/deblurring models for hyperspectral material identification, *Numerical Linear Algebra With Applications* 19 (1) (2012) 153–173 (2012).
- [8] X.-L. Zhao, F. Wang, T.-Z. Huang, M. K. Ng, R. J. Plemmons, Deblurring and sparse unmixing for hyperspectral images, *IEEE Transactions on Geoscience and Remote Sensing* 51 (7) (2013) 4045–4058 (2013).
- [9] N. Li, B.-X. Li, Tensor completion for on-board compression of hyperspectral images, *Proceedings of IEEE International Conference on Image Processing* (2010) 517–520 (2010).
- [10] Z.-M. Xing, M.-Y. Zhou, A. Castrodad, G. Sapiro, L. Carin, Dictionary learning for noisy and incomplete hyperspectral images, *SIAM Journal on Imaging Sciences* 5 (1) (2012) 33–56 (2012).
- [11] J.-T. Sun, H.-J. Zeng, H. Liu, Y.-C. Lu, Z. Chen, Cubesvd: a novel approach to personalized web search, *Proceedings of International World Wide Web Conferences* (2005) 382–390 (2005).
- [12] T. G. Kolda, B. W. Bader, J. P. Kenny, Higher-order web link analysis using multilinear algebra, *Proceedings of IEEE International Conference on Data Mining* (2005) 242–249 (2005).

- [13] N. Varghees, M. Manikandan, R. G. John, Adaptive mri image denoising using total-variation and local noise estimation, Proceedings of IEEE International Conference on Advances in Engineering, Science and Management (2012) 506–511 (01 2012).
- [14] N. Kreimer, M. D. Sacchi, A tensor higher-order singular value decomposition for prestack seismic data noise reduction and interpolation, *Geophysics* 77 (3) (2012) 113–122 (2012).
- [15] R. A. Harshman, Foundations of the parafac procedure: Models and conditions for an “explanatory” multi-modal factor analysis, *UCLA Working Papers in Phonetics* (1970).
- [16] L. R. Tucker, Some mathematical notes on three-mode factor analysis, *Psychometrika* 31 (3) (1966) 279–311 (1966).
- [17] M. E. Kilmer, C. D. M. Martin, Factorization strategies for third-order tensors, *Linear Algebra and its Applications* 435 (3) (2011) 641–658 (2011).
- [18] C. D. Martin, R. Shafer, B. Larue, An order- p tensor factorization with applications in imaging, *SIAM Journal on Scientific Computing* 35 (2013) 474–490 (2013).
- [19] M. E. Kilmer, K. S. Braman, N. Hao, R. C. Hoover, Third-order tensors as operators on matrices: A theoretical and computational framework with applications in imaging, *SIAM Journal on Matrix Analysis and Applications* 34 (1) (2013) 148–172 (2013).
- [20] M. K. Ng, R. H. Chan, W. Tang, A fast algorithm for deblurring models with neumann boundary conditions, *SIAM Journal on Scientific Computing* 21 (3) (1999) 851–866 (1999).
- [21] Z.-M. Zhang, G. Ely, S. Aeron, H. Ning, M. E. Kilmer, Novel methods for multilinear data completion and de-noising based on tensor-svd, *Proceedings of Computer Vision and Pattern Recognition* (2014) 3842–3849 (2014).
- [22] C.-Y. Lu, J.-S. Feng, Y.-D. Chen, W. Liu, Z.-C. Lin, S.-C. Yan, Tensor robust principal component analysis: Exact recovery of corrupted low-rank tensors via convex optimization, *Proceedings of Computer Vision and Pattern Recognition* (2016) 5249–5257 (2016).
- [23] O. Semerci, H. Ning, M. E. Kilmer, E. L. Miller, Tensor-based formulation and nuclear norm regularization for multienergy computed tomography, *IEEE Transactions on Image Processing* 23 (4) (2014) 1678–1693 (2014).
- [24] S. Boyd, N. Parikh, E. Chu, B. Peleato, J. Eckstein, Distributed optimization and statistical learning via the alternating direction method of multipliers, *Found. Trends Mach. Learn.* 3 (1) (2011) 1–122 (Jan. 2011).
- [25] Z.-C. Lin, M.-M. Chen, Y. Ma, L.-Q. Wu, The Augmented Lagrange Multiplier Method for Exact Recovery of Corrupted Low-Rank Matrices, *ArXiv e-prints* (Sep. 2010). arXiv:1009.5055.
- [26] B.-S. He, M. Tao, X.-M. Yuan, Alternating direction method with gaussian back substitution for separable convex programming, *SIAM Journal on Optimization* 22 (2) (2012) 313–340 (2012).
- [27] M. V. Afonso, J. M. Bioucasdias, M. A. T. Figueiredo, An augmented lagrangian approach to the constrained optimization formulation of imaging inverse problems, *IEEE Transactions on Image Processing* 20 (3) (2011) 681–695 (2011).
- [28] D.-R. Han, X.-M. Yuan, A note on the alternating direction method of multipliers, *Journal of Optimization Theory and Applications* 155 (1) (2012) 227–238 (2012).